International Journal of Mechanical Sciences 305 (2025) 110781

Contents lists available at ScienceDirect

International Journal of Mechanical Sciences

journal homepage: www.elsevier.com/locate/ijmecsci

Development of a capillary-driven two-phase microcooler using copper wiremesh 3D manifold and silicon micropin fin wicks

Daeyoung Kong [a], Roman Giglio [b], Muhammad R. Shattique [c], Qianying Wu [a], Heungdong Kwon [a], James W. Palko [b], Hyoungsoon Lee [d], Ercan M. Dede [e], Mehdi Asheghi [a], Kenneth E. Goodson [a,1,*]

[a] Department of Mechanical Engineering, Stanford University, Stanford, CA, 94305 USA
[b] Department of Mechanical Engineering, UC Merced, Merced, CA, 95340 USA
[c] Materials and Biomaterials Science and Engineering Graduate Program, University of California Merced, Merced, CA, 95340 USA
[d] Department of Mechanical Engineering, Chung-Ang University, Seoul, 06974 South Korea
[e] Electronics Research Department, Toyota Research Institute of North America, Ann Arbor, MI, 48105 USA

ARTICLE INFO

Keywords:
Thermal management
Electronics cooling
Capillary-driven
Thin-film boiling
Micropin fin wick
Copper wiremesh manifold

ABSTRACT

Sustainable and energy-efficient cooling is crucial for managing high-performance computing architectures within the rapidly expanding data center industry. Here, we introduce a novel capillary-driven two-phase microcooler that eliminates the need for conventional pump-based cooling schemes. The device integrates thin-film boiling in silicon micropin fin wicks (six geometric variations) with a copper 3D wiremesh manifold (two spacings), representing a new approach that combines self-regulated capillary liquid supply with nearly complete vapor phase separation. Using deionized water, the optimized wick achieved a critical heat flux of 486 W/cm^2 at a low superheat of $\Delta T_{sat} = 7$ °C, corresponding to a two-phase thermal resistance of $R''_{tp}= 1.8$ mm^2- °C/W, while ensuring nearly complete liquid–vapor separation (vapor quality ~0.9). The microcooler offers design flexibility that allows any combinations of wick and manifold materials 9silicon or copper) as well as area and performance scalability toward larger heated footprints and higher heat fluxes (~1 kW/cm^2) and heat transfer coefficients (~10^6 W/m^2- °C). These findings establish capillary-driven two-phase cooling as a transformative pathway for the thermal management of high-end microelectronics and energy-efficient data centers.

1. Introduction

US data centers currently consume ~200 terawatt-hours per year, with cooling requirements accounting for 20–30 % of this total [1]. Transformational, sustainable, and energy-efficient cooling technologies [2,3] are needed to reduce the energy requirements [4,5]. Conventionally, air and liquid cooling solutions [6–9] have been extensively implemented in data center thermal management; however, the large thermal resistance between the junction and inlet coolants (<20 °C) requires a refrigeration system that significantly increases cooling power requirements. In order for lowering the thermal resistance, immersion cooling [10–14], heat pipes [15–19], and vapor chambers [20–23] have been commonly used as passive cooling solutions [24,25]. However, these approaches are generally limited to low-to-intermediate power densities (up to 200 W/cm^2). Consequently, pumped two-phase cooling has been explored for higher heat fluxes; yet practical deployment still remains challenging because the required pressure drops are large and the flow is susceptible to dynamic and static instabilities at modest vapor qualities ~ 0.3 [26,27]. More recently, capillary-driven thin-film boiling emerges as an effective solution for energy-efficient two-phase cooling utilizing wire mesh wicks [28–33], sintered copper wicks [34–38], nanowires [39–43], and microstructures [44–47] due to the rapid transport of liquid to the heated surfaces and ensuring efficient vapor evacuation at higher vapor qualities > 0.8. In addition, unprecedented heat dissipation level up to 1400 W/cm^2 at superheats of ~10 °C have been demonstrated on narrow heaters with lateral dimensions of 250–500 μm [48,49]. Nonetheless, studies on capillary-driven micro-coolers that can be manufactured across large footprint area while meeting real-world GPU packaging requirements remain limited. Moreover, the outstanding thermal performance shown in small-scale prototypes must be achieved over full die-scale footprints [50,51].

* Corresponding author.
E-mail address: goodson@stanford.edu (K.E. Goodson).
[1] Website: http://nanoheat.stanford.edu/

https://doi.org/10.1016/j.ijmecsci.2025.110781
Received 24 March 2025; Received in revised form 27 August 2025; Accepted 30 August 2025
Available online 1 September 2025

Nomenclature

A_c	cross-sectional area [m^2]
A_{fin}	fined surface area [m^2]
A_h	heated area [m^2]
C_p	specific heat [J/kg-K]
CHF	critical heat flux [W/m^2]
D_f	diameter of fin [m]
g	acceleration due to gravity [m/s^2]
H_f	height of fin [m]
h_{lv}	latent heat [J/kg]
K	permeability [m^2]
k	thermal conductivity [W/m-K]
l_h	heater length [m]
l_{eff}	effective wicking length [m]
$\dot{m}$	mass flow rate [kg/s]
P	pitch of fin [m]
P_{liq}	viscous pressure of liquid [Pa]
P_{cap}	capillary pressure [Pa]
q	heat dissipation rate [W]
q''	heat flux [W/m^2]
R''	thermal resistance [m^2- °C/W]
T_h	heater surface temperature [°C]
T_{wick}	wicked surface temperature [°C]
ΔT_{sat}	superheat temperature [°C]
t	thickness [m]
W_{mani}	manifold pitch [m]
x_e	exit quality [-]

Greek symbols

θ	apparent contact angle [deg.]
μ	dynamic viscosity [Pa-s]
ρ	density [kg/m^3]
σ	surface tension [N/m]

Subscripts

cap	capillary
CHF	critical heat flux
in	inlet
input	input
loss	loss
lc	liquid channel
sat	saturation
Si	silicon
SiO_2	silicon dioxide
sp	single-phase
tp	two-phase
vc	vapor channel

Motivated by advances in 3D-manifold approaches to forced-convection cooling [52–56], recent studies have introduced millimeter-scale 3D-manifold designs that realize capillary-driven flow [57–60]. Giglio et al. [58] assembled stacks of copper wire mesh/spacer pairs to construct a capillary-based 3D manifold for cooling to remove 500 W/cm^2 from laser processed aluminum nitride (AlN) pyramidal fins (wick) over an area of 5 × 5 mm^2 achieving a superheat of 35 °C and minimal thermal resistance of 7.5 mm^2- °C/W. In this approach, the copper wire mesh is simply placed over the AlN wick heated area, which is dipped in boiling water. The water is wicked via copper wire mesh plates towards the manifold center and down to the heated area, where it is converted to vapor and exits rapidly from the space between the 3D manifold's wire mesh plates. When the free-standing, three-dimensional copper wire-mesh manifold is immersed in a pool of heated water, liquid is drawn into the manifold while vapor escapes. This cyclical inflow floods portions of the heated surface, leading to the relatively high measured superheat of 30–45 °C. Previously, Shattique et al. [59] measured water permeability of free-standing copper #100 wire meshes at varying capillary pressures demonstrating that the relative permeability of the copper wire mesh with plain weave is not effected severely until 600 Pa of capillary pressure but it can fall sharply beyond this limit. Heungdong et al. [60–62] fabricated a unique area-scalable open channel silicon-based 3D manifold that allows liquid wicking from the side plenums and delivery over an area of 5 × 5 mm^2 [60], 10×10 mm^2 [61] and 20×20 mm^2 [62]. This novel 3D manifold can support hybrid single and/or two-phase cooling depending on the inlet coolant flowrate and temperature, and heat flux levels [61]. More recently, Li et al. [63] introduced hierarchically ordered perforated wire meshes that enable low-resistance liquid wicking, rapid bubble nucleation, and directional vapor escape. Their work showed the scalability and versatility of this capillary-driven perforated surface strategy across various micro/nano-structured surfaces, achieving lowest thermal resistance of 3.2 mm^2- °C/W and high critical heat flux of 311 W/cm^2 on compact heating areas of 10×10 mm^2. Lu et al. [64] demonstrated enhanced thin film boiling using a capillary-driven configuration enabled by a super-hydrophilic copper mesh wick, achieving heat fluxes up to 166 W/cm^2 with high thermal stability. Their work emphasized the importance of promoting directional vapor escape and maintaining ultrathin film integrity through in-plane wicking, which suppresses dryout even under high heat flux. This study also highlighted the role of mesh geometry and wettability in optimizing boiling performance for high-power cooling applications.

Advanced capillary-driven two-phase cooling using wiremesh-based liquid supply architectures has developed, but the field still lacks a comprehensive characterization of micro-wick behavior and a clear understanding of how manifold-channel pitch on the wick governs thermal–hydraulic performance. Addressing this gap requires controlled parametric experiments and models that decouple wick properties from manifold geometry.

In this study, we utilized the capillary-based 3D copper wire mesh manifold developed by Giglio et al. [58] alongside several silicon micropin fin evaporator wicks to achieve complete liquid-vapor phase separation, reaching vapor quality levels up to 0.9. This was accomplished by precisely controlling the delivery of water coolant to the manifold rather than submerging it in boiling water, thereby preventing flooding of the heated region, which exacerbated superheat. We further tested eight combinations of silicon pin fin wick (D_f= 4–20 μm, H_f= 100–200 μm, P = 16–46 μm) and 3D copper wiremesh designs with wiremesh spacings (I.e. pitch between layers) of 550 and 650 μm to better understand the impact of geometry and flow conditions on the micro-cooler's performance. We achieved high heat flux level of ~500 W/cm^2 and superheat levels of 7–15 °C, thermal resistance of 1.8 mm^2- °C/W with a very small coolant flow rate of $\dot{m}$ = 3 g/min, which is 10 times smaller than conventional single-phase microchannel cooling [65, 66].

2. Experimental section

This section describes the fabrication and assembly process for sinter-bonded copper wire-mesh manifold and the silicon micro-pin-fin wicks followed by description of the experiment set up, and finally details of data reduction combined with the uncertainty analysis.

2.1. Fabrication of wire mesh manifold

The three-dimensional copper wire mesh manifold illustrated in

Fig. 1(a) comprises stacked layers of #100 copper mesh, featuring wire diameters and openings of 125 μm and a thickness of 250 μm, and mesh spacing of 550 μm or 650 μm using solid copper spacers. The assembly is bonded through a sintering process, which involves heating to 800 °C for one hour, followed by cleaning with deionized water and isopropyl alcohol. Fig. 1(b) and (c) depict a conceptual model of a capillary-based microcooler. This microcooler incorporates the three-dimensional copper wire mesh manifold, which is positioned atop (but not bonded to) a silicon pin fin wick evaporator. This configuration is critically important as it allows for the use of various combinations of wicking structures and manifold materials without concerns about thermal mismatch between the wick and the manifold. The microcooler has overall dimensions of 8 × 5 × 25 mm^3, although its volume can be substantially reduced to facilitate packaging and integration. In the manifold, the mesh plates are vertically aligned, enabling liquid to be wicked from the side reservoirs toward the center and then downward to the heated area, which measures 5 × 5 mm^2, as shown in Fig. 1(b) and (c). It is noteworthy that water bridges the gap between the three-dimensional manifold and the wick structure. The size of the gap is much smaller than the mesh openings. The water delivered to the porous evaporator is wicked laterally, subsequently converted to vapor, and then exits through the gaps between the copper wire mesh layers, as indicated by the red arrows in Fig. 1(d).

A significant design improvement over the previous study [58] involves the controlled delivery of coolant water using a ¼-inch polyurethane tube inserted into large circular openings at both ends of the 3D manifold (Fig. 1(a)). The tube ends were sealed, and small slits were fabricated in the polyurethane tubes. When the water within the tubes is pressurized using a syringe pump, the tubes expand, causing the slits to open (Fig. 1(b)). This mechanism allows for the gradual and controlled delivery of liquid coolant to the copper wire mesh layers. It is noted that the syringe pump was employed solely to enable precise control of the flow rate to the copper wire-mesh micro-cooler; in practical data-center deployments the device is intended to operate passively, without any pump-assisted liquid delivery. Fig. 1(e) presents a bottom view of the copper wire mesh sheets that are in contact with the silicon pin fin wick evaporator. Two types of copper wire mesh 3D manifolds were utilized, featuring different nominal center-to-center spacings of 550 μm and 650 μm, which determine the width of the vapor exit channels. Notably, the unique design of the 3D manifold completely separates the pathways for liquid delivery (through the copper wire mesh) and vapor exit (the space between the wire mesh plates). This separation results in complete liquid-vapor phase separation, achieving a vapor exit quality ∼ 0.9.

2.2. Integration of silicon wicks with manifold

The silicon micropin fin evaporators were fabricated using the deep reactive ion etching (DRIE) process on a 500 μm silicon substarte over an area of 5 × 5 mm^2 on a 20×20 mm^2. The pin fins nominal dimensions are: D_f = 4, 11, and 20 μm in diameter, P = 16, 30 and 46 μm in spacing, and H_f = 100 and 200 μm in height. A thin metal heater, comprising 20 nm of titanium (Ti) and 300 nm of platinum (Pt), were sequentially patterned on the backside of the pin fin wick substrate using electron-beam (e-beam) evaporation to generate heat. In this study, a calibrated infrared (IR) camera was utilized for thermal imaging of the entire heated area to assess the uniformity of temperature distribution over the 5 × 5 mm^2 region. Additionally, a 3D-printed sample holder with drainage holes (see Fig. 1(b)) was fabricated to minimize misalignment between the copper wire mesh manifold and the silicon pin fin wick evaporator. The test matrix employed for characterizing the micro-cooler performance is presented in Table 1.

2.3. Test procedure and uncertainty

Thermofluidic evaluations of the silicon capillary-based micro-cooler were performed utilizing a simple open-loop configuration, as depicted in Fig. 2. The micro-cooler functions through capillary-driven flow within both the manifold and the porous wick. To ensure precise regulation of deionized water at 20 °C supplied to the copper wire mesh three-dimensional manifold, a double-barrel syringe pump (PHD-2000, Harvard Apparatus) with a total capacity of 300 mL was employed, operating at flow rates of 5, 10, and 15 g/min. The fluid temperature and absolute pressure at the micro-cooler inlet were monitored using Type-K thermocouples (OMEGA KMQSS-062) and a pressure transducer

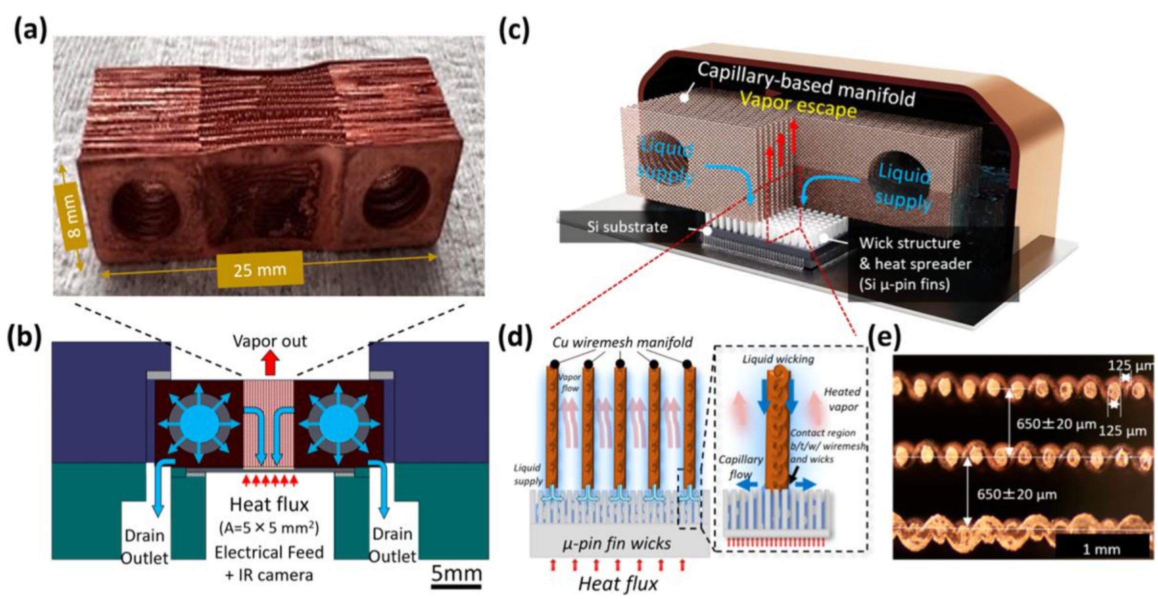

Fig. 1. Capillary-based micro-cooler using silicon pin fin wick and copper wire mesh manifold. (a) An image of the as-fabricated copper wire mesh manifold. Total dimension of wire mesh manifold consists of 5 × 25×8 mm^3. (b) Schematic of micro-cooler integrated with copper wire mesh manifold. Two drain through-holes help to prevent excessive liquid delivery into the wick and maintain an adequate thin liquid film. (c) Graphical image of test module for the micro-cooler. (d) Capillary action in the porous wire-mesh and micropillar-wick structures continuously supplies liquid to the local hotspots, while the vapor produced at elevated heat flux readily vents through the mesh interstices, thereby promoting efficient liquid–vapor separation. (e) There are two spacing of copper wire mesh manifold in this study: 550 μm and 650 μm (shown in the picture), wire mesh diameter and spacing between wires are both 125 μm.

Table 1
Dimensions of the silicon pin fin wicks and manifold in microns. (unit: μm).

Micropin fin wick					3D Manifold
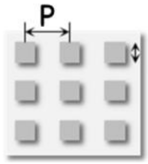	Diameter D_f	Pitch P	Height H_f	Fin Area/ Heater Area, A_{fin}/A_h	Manifold Width W_{mani}
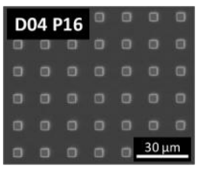	4.3	16	106	7.7	550 650
			192	13.1	550 N/A
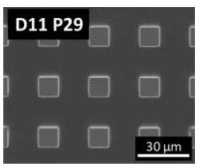	11	30	113	6.9	N/A 650
			200	11.5	550 N/A
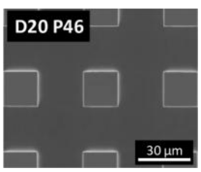	20	46	115	5.4	550 650
			208	9.0	550 N/A

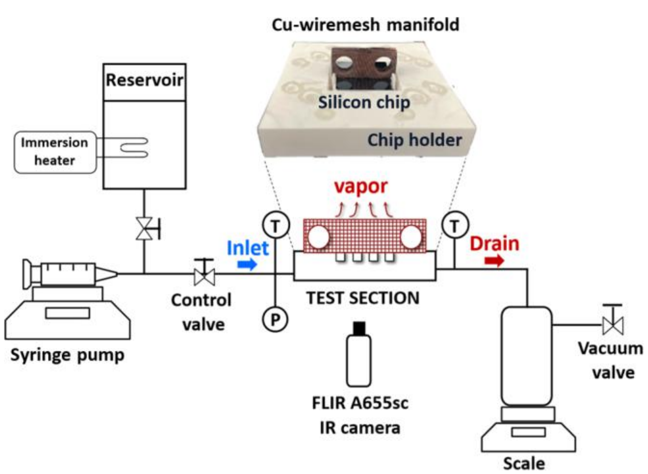

Fig. 2. .Simplified open flow loop system. The water in the reservoir is first degassed using an immersion heater. A syringe pump then delivers the targeted volumetric flow rate. A precision balance positioned at the loop outlet records mass loss of the drained water, enabling accurate determination of the vaporization rate during thermal testing. An infrared camera monitors the wick's backside heater temperature throughout the experiment.

(PX300–015G5V, OMEGA), respectively. Furthermore, the temperature at the surface of the heated chip was recorded via an infrared (IR) camera (A655sc, FLIR). The syringe pump continuously supplies coolant to the wire mesh plenums situated on either side of the active region. A portion of the water is drawn into the plenum through the copper wiremesh screen, while the surplus water exits the 3D manifold and is subsequently removed through drainage holes. The volume of drained fluid is influenced by the syringe pump's flow rate, the liquid delivery configuration, and the geometry of both the 3D manifold and the plenums. Flow rates were quantified by weighing the drained water using a scale (PI-225D, Denver Instrument), with measurements averaged over 60-second intervals. Thermal testing was conducted by progressively increasing the heat flux in increments of 40 W/cm^2 using a programmable power supply (XLN15015, BK Precision). The testing procedure was terminated when a rapid and significant rise in the heater temperature occurred within a short timeframe, signifying a failure or the cooling performance limit. The effective heat flux was determined based on electrical Joule heating ($q_{input} = V \times I$) after subtracting the heat losses (q_{loss}),

$$q''_{tot} = \frac{q_{input} - q_{loss}}{A_h}. \tag{1}$$

The heat loss was estimated to be below 12 % for single-phase flow/ evaporation and under 6 % for two-phase flow, with comprehensive details provided in **Supplementary materials, Section A**. The temperature of the micropin fin wick surface (T_{wick}) was determined using infrared (IR) thermometry of the heater chip surface, based on the assumption of one-dimensional heat conduction through the thickness of the silicon substrate:

$$T_{wick} = T_h - q''_{tot}\left(\frac{t_{Si}}{k_{Si}} + \frac{t_{SiO_2}}{k_{SiO_2}}\right), \tag{2}$$

where t_{Si} and k_{Si} are the thickness (~400 μm) and thermal conductivity (115 W/m-K at 100 °C) of silicon substrate. t_{SiO_2} and k_{SiO_2} are the thickness (0.5 μm) and thermal conductivity (1.4 W/m-K) of silicon dioxide for electrical passivation layer.

The water mass flow rate entering the silicon pin fin wick ($\dot{m}_{cap,sp}$), which is strictly driven by capillary forces of wiremesh manifold, was evaluated from a sensible heat energy balance applied within the single-phase/evaporation regime. Consequently, a portion of the applied heat is utilized to raise the temperature of the liquid from the inlet temperature, T_{in}=22 °C, to the saturation temperature of 100 °C. The required sensible heat is therefore estimated by:

$$q''_{sp,cap} = \frac{\dot{m}_{cap,sp} C_p (T_{sat} - T_{in})}{A_h}, \tag{3}$$

where C_p denotes the specific heat capacity of water evaluated at the mean temperature between the saturation temperature and the inlet temperature. The heat absorbed by the coolant during the phase change from liquid to vapor is defined as:

$$q''_{tp} = q''_{tot} - q''_{sp,cap}. \tag{4}$$

The steady-state two-phase thermal resistance is defined as:

$$R''_{tp} = \frac{T_{wick} - T_{sat}}{q''_{tp}}, \tag{5}$$

where T_{sat} is the saturated temperature of water (100 °C in this study). At heat fluxes approaching the critical heat flux (CHF), the exit quality, x_e, can be approximately estimated by taking the ratio of the two-phase mass-flow rate to the corresponding single-phase/evaporation mass flow rate:

$$x_e = \frac{\dot{m}_{cap,tp}}{\dot{m}_{cap,sp}}, \tag{6}$$

where $\dot{m}_{cap,tp}$ represents the two-phase mass flow rate through the wick during boiling. Experimentally, it is determined by subtracting the drained flow rate from the pump-inlet flow rate, i.e. $\dot{m}_{cap,tp}= \dot{m}_{in,pump}$ - $\dot{m}_{out,drain}$.

The measurement uncertainty associated with electrical heating, q, is estimated to be below 0.1 %. Inlet and heater temperatures, measured using a thermocouple and an infrared camera, exhibit accuracies of ±1 °C and ±2 %, respectively. The uncertainties in the pumped liquid mass flow rate and the drained liquid mass, as determined by the syringe pump and digital scale, are estimated to be ±0.35 % and ±0.1 g, respectively. Utilizing standard error analysis, the propagated uncertainty of the effective heat flux is calculated to be <5 %, while the uncertainty in the wicking surface temperature is estimated to be within 7 %. Additionally, the accuracy of the two-phase heat flux is assessed to be within 7 %, and the maximum uncertainty in the two-phase thermal resistance is below 8 %. Finally, the uncertainty in exit quality is determined to be below 8 %.

3. Results and discussion

This section presents the boiling curve characteristics, depicting transition from single-phase/evaporation to mixed and then fully two-phase flow. We then explored the impact of pin-fin wick and copper wiremesh 3D manifold geometry on thermal performance of the microcoolers. A narrower vapor-exit channel and a well-designed silicon pin fin wick allows for optimum liquid delivery and vapor extraction resulting in lower thermal resistance and superheat and highest CHF levels. Finally, all results are gathered into one heat flux versus thermal resistance plot, leading to clear, easy-to-follow design rules for optimum wick properties and manifold spacing.

3.1. Two-phase performance on capillary-driven micro-cooler

3.1.1. General features

In this study, we utilize a capillary-driven 3D copper wire mesh manifold, developed by Giglio et al. [58], integrated with a silicon micropin fin evaporator wick to achieve complete liquid-vapor phase separation. Before examining a complete set of performance data for various combinations of micropin fin wicks and 3D manifolds (see Table 2 and Table 3), we first examine the key characteristics of this unique microcooler. Fig. 3 depicts heat flux vs. "spatially averaged" wick temperature for three distinct single-phase/evaporation, mixed or hybrid single-phase/evaporation and two phase boiling, and finally two-phase boiling regimes. The single-phase/ evaporation linear regime exists in the temperature range of 22 °C to ~ 80 °C. In this regime, the coolant remains in single-phase within the silicon pin fin array while thin film evaporation prevails mainly at the tip of the silicon pin fins as well as surface of the water in between the pin fins [67]. Finally, the two-phase boiling regime emerges once the wick temperature exceeds 105 °C and is nearly independent of the heat flux. A mixed or hybrid single-phase/evaporation and two phase condition exists in the temperature range of ~90 to 105 °C where the single-phase/evaporation exists at the left and right inlet regions while two-phase boiling prevails in the interior regions (see IR images in Fig. 4).

The results indicate that the flow is capillary driven within both the manifold and the evaporator wick. It is important to note that, irrespective of the pumped mass flow rate ($\dot{m}_{in,pump}$) supplied to the copper wire mesh manifold at the inlet, the heater input is precisely balanced by the mass flow rate ($\dot{m}_{cap,tp}$) driven by capillary forces to sustain two-phase boiling. Any excess flow ($\dot{m}_{out,drain}$) is drained, as noted in the inset of Fig. 3. Furthermore, the extent of excess water dranage, $\dot{m}_{out,drain}$ depends on the geometry of the copper wire mesh manifold and effective wire mesh permeability among other factors, and can be improved in the future design iterations. At $\dot{m}_{in,pump}$= 15.7 g/min, the highest critical heat flux CHF of 486 W/cm² is achieved consuming $\dot{m}_{cap,tp}$~2.9 ± 0.2 g/min, resulting in a vapor quality of approximately 0.90±0.05. Similarly, for $\dot{m}_{in,pump}$= 5.3 and 11.3 g/min, the CHFs and vapor exit qualities are 350 and 464 W/cm², and 0.75±0.02 and 0.84±0.03, respectively. This indicates that there is not enough supply of liquid to be utilized by the copper wire mesh due to excessive drainage from the left and right sections of the wire mesh manifold where the plastic tubes are connected.

Notably, the superheat across all tested mass flow rates ranges between 7 and 9 °C, indicative of thin film boiling within the silicon wick. The non-uniform heating from the serpentine heaters due to current concentration at the corners resulted in formation of localized hotspots exceeding ~1 kW/cm² over ~150 µm × 150 µm (see Fig. 4). Additionally, the design of the plenums, which supply coolant from both left and right sides (Fig. 1(b)), exacerbates temperature non-uniformity due to low coolant inlet temperature of 22 °C.

Preliminary results from a more recent work from this group [68] for 5 × 10 mm² copper wiremesh footprint and 5 × 5 mm² heated area, yielded similar results for q'' vs. T_{wick} and CHF limit, indicating that the copper wire mesh 3D is not limiting factor in delivery of the water to the hot spots. We concluded that the CHF is limited by the capillary flow resistance in the silicon pin fins rather than the capacity of the 3D manifold to deliver coolant to the 5 × 5 mm² heated area.

3.1.2. Effect of pin fin wicks on thermal performance

Here, we conducted systematic tests to evaluate the influence of pin fin geometry on the thermal performance of the micro-cooler, utilizing a copper wire mesh 3D manifold with a fixed mesh spacing of W_{mani}= 650 µm (see Fig. 5 and Table 2). The three pin fin configurations vary by diameter and spacing of them (see Table 1): D04P16 (High density), D11P29 (medium density), and D20P46-M650 (low density) at the inlet flow rate of 15 g/min. Clearly, the geometry of the pin fin wick significantly impacts the CHF values: For case A (dense fins), the CHF is likely limited by the capillary flow resistance while for case C (sparse fins), there may not be sufficient capillary pressure to sustain the capillary flow; finally, for case B, either the capillary resistance in the Cu wire mesh 3D manifold or silicon pin wick could be the limiting factor, the latter is under investigation [68]. A similar trend is observed for inlet mass flow rates of 5 and 10 g/min (**Supplementary materials, Section B**).

Clearly, the D11P29-M650 configuration (case B) demonstrates the best performance (see Fig. 3), resulting in both higher CHF of 486 W/cm² and lower superheat level of 7.3 °C, achieving an effective two-phase thermal resistance of 1.8 mm²- °C/W (see Table 2). This is comparable to the intrinsic conduction thermal resistance of a 200 µm thick silicon substrate ~ 2 mm²- °C/W. Also, the vapor exit quality for case B is x_e= 0.89±0.05 compared to 0.45±0.04 and 0.56±0.03 for cases A and C, respectively. In the current study, water at 22 °C is used, resulting in a single-phase liquid delivery in the wick and evaporation at the tip of the silicon pin fins and water in between. A recent study indicated that by utilizing a saturated liquid "coolant" near 100 °C, the linear single-phase region vanishes and a fully two-phase regime would prevail but the critical heat flux remains the same as that with the water introduced at 22 °C [68]. This implies that for a fully two-phase cooler even lower thermal resistance of 1.5 mm²- °C/W can be achieved for the Case B (refer to Table 2, last column).

Table 2
Summary table of thermal test results for copper wire mesh spacing of, W_{mani}= 650 µm, and micropin fin wicks. D**P**-M***, represents diameter and pitch of wick and manifold spacing pairs.

Design	W_{mani}	H_{fin}	$\dot{m}_{in,pump}$	$\dot{m}_{out,drain}$	$\dot{m}_{cap,tp}$	q''_{CHF}	q''_{tp}	$\dot{m}_{cap,tp,cal}$	x_e	$\eta_{fin,CHF}$	$T_{wick,CHF}$	$R''_{tp,CHF}$ @ T_{in}= 22 °C	$R''_{tp,CHF,cal}$ @ T_{in}= 100 °C
	µm		g/min			W/cm²		g/min	–	–	°C	mm²- °C/W	
D04P16-M650	650	106	15.1	13.5	1.7 ± 0.14	268	181	1.2	0.45±0.04	0.69	116	8.7	5.9
D11P29-M650	650	113	15.7	12.8	2.9 ± 0.16	486	413	2.7	0.89±0.05	0.45	107	1.8	1.5
D20P46-M650	650	115	15.7	13.7	2.0 ± 0.1	316	237	1.6	0.56±0.03	0.82	115	6.6	5.0

Table 3
Enhanced two-phase heat transfer by the reduced spacing of copper wiremesh manifold (W_{mani}= 550 µm).

Design	W_{mani}	H_{fin}	$\dot{m}_{in,pump}$	$\dot{m}_{out,drain}$	$\dot{m}_{cap,tp}$	q''_{CHF}	q''_{tp}	$\dot{m}_{cap,tp,cal}$	x_e	$\eta_{fin,CHF}$	$T_{wick,CHF}$	$R''_{tp,CHF}$ @ T_{in}= 22 °C	$R''_{tp,CHF,cal}$ @T_{in}= 100 °C
Unit	µm		g/min			W/cm²		g/min	–	–	°C	mm²- °C/W	
D04P16-M550	550	106	15.1	12.6	2.3 ± 0.05	376	285	1.90	0.57±0.01	0.54	114	5.0	3.8
D20P46-M550	550	115	15.7	12.6	2.7 ± 0.07	487	401	2.67	0.70±0.02	0.67	112	3.0	2.5

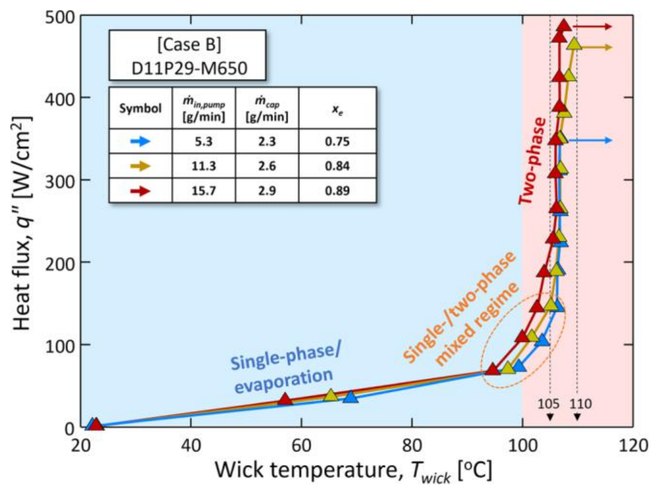

Fig. 3. .Thermal performance (heat flux vs. spatially averaged wick temperature) as a function of mass flow rate delivered to the copper wire mesh manifold. The boiling curve at each flow rate of ~ 5, 10 and 15 g/min yielded CHFs of 350, 560 and 486 W/cm², respectively. For the highest heat flux of 486 W/cm², the vapor exit quality, x_e ~0.9, superheat ΔT_{sat} ~9.0 ± 2 °C. The inset table represents key performances parameters at CHF; for details refer to Table 2.

Also it is noteworthy that superheat levels in cases A and C (ΔT_{sat}=16 °C) are nearly double that of case B (ΔT_{sat}= 7.4 °C) likely due to increased temperature instability and formation of hot spots (see IR images of the silicon heater chip in Fig. 6). Once a hotspot is formed, there may not be sufficient permeability to rewet the wick in case A, leading to a sharp temperature spike and resulting in an early onset of CHF similar to the local dry-out mechanism observed in pool boiling [69,70]. (see **Supplementary materials, Section C**). In contrast, sparse structures like D20P46 of case C experience lower capillary pressure; both can lead to reduce the rewetting speed and result in lower dry-out levels (see **Supplementary materials, Section D**).

3.1.3. The impact of wiremesh spacing in the 3D manifold

The effective wicking length, l_{eff}, determines the optimum copper wiremesh spacing (vapor exit channel width, $W_{mani,vc}$) as illustrated in Fig. 7. The effective wicking length, l_{eff}, defined as the distance at which the maximum CHF can be achieved in a wicking structure, is the critical factor in evaluating the thermal performance of the capillary-based microcooler; the relationship between maximum CHF and l_{eff} is derived as [49]:

$$q''_{CHF,max} = \frac{4\xi K A_c \sigma \rho_f h_{fg} cos\theta}{\mu_f l_{eff}\left(l_h l_{eff}\right)\left(\frac{4}{\pi}\left(\frac{P}{D}\right)^2 - 1\right)}, \quad (7)$$

where ρ_l, μ_l, σ, h_{fg}, and θ are the liquid density, liquid dynamic viscosity, surface tension, latent heat of water, and contact angle, respectively. K is the permeability of the pin fin wick. For estimating the liquid permeability, empirical correlation has been utilized from previous study [71]. A_c is the cross-sectional area of pin fin wick and l_h is the total heater length. ξ is the coefficient for the liquid fraction in the wick during the boiling. Please refer to **Supplementary materials, Section E** for a more detailed derivation of the CHF modeling [49].

It is noted that the effective wicking length, l_{eff}, is an intrinsic property of the wick and coolant not the 3D manifold copper wire mesh spacing. If $W_{mani,vc}$ exceeds $2l_{eff}$ (i.e., $W_{mani,vc} > 2l_{eff}$), dry-out in the evaporator occurs at the center of the wick (see Fig. 7(c)). Conversely, if $W_{mani,vc}$ is equal to or $<2l_{eff}$ (i.e., $W_{mani,vc} \leq 2l_{eff}$), higher CHF levels in the evaporator wick can be achieved due to the sustained liquid thin-film as shown in Fig. 7(d) and (e).

For a practical design of a capillary-based micro-cooler, it's important to note that the copper wiremesh layers delivering the liquid to the heated area also occupy space, thereby reducing the effective area available for capillary boiling across the total heated chip area:

$$q''_{CHF,\mu-cooler} = \left(\frac{W_{mani,vc} - W_{mani,lc}}{W_{mani,vc} + W_{mani,lc}}\right) q''_{CHF}. \quad (8)$$

Consequently, there is a limit to how high the total effective CHF of the heater chip can be as shown in Fig. 7(e). For further details, reference [72] provides a comprehensive illustration of the optimization process, which takes into account both the effective wicking length and the spatial footprint occupied by the copper wire mesh.

Fig. 8 shows the results of the thermal performance tests for two types of 3D manifolds with copper wiremesh spacing of 550 µm and 650 µm, and two pin fin wick types, D04P16 and D20P46 (see Table 3 for details) at constant mass flow rate of 15 g/min. The results demonstrate that, for both types of silicon pin fin wicks, a reduced manifold spacing of 550 µm leads to significantly higher CHF levels—ranging from a 40 % to 60 % increase—and lower superheat levels. This behavior suggests the presence of thin-film capillary wicking within the silicon pin fin structures, as evidenced by the infrared thermal images provided in **Supplementary materials, Section F**. In addition, it implies that narrowing the spacing between wiremesh layers can improve boiling performance while overall dense mesh layers diminish the effective boiling area and ultimately degrade heat transfer. Accordingly, there exists an optimal spacing that balances this trade-off and maximizes overall thermal performance. For a detailed discussion on the influence of pin fin wick height on thermal performance, refer to **Supplementary materials, Section G**.

3.2. Evaluation of two-phase thermal performance

Fig. 9 presents a comparative analysis of two-phase thermal resistance as a function of CHF across five different micro-cooler configurations tested in this study. Each data point is annotated with the corresponding capillary mass flow rate, $\dot{m}_{cap,tp}$, and exit vapor quality within a bounding box.

For the dense D04P16-M650 wick design, characterized by a short wick height of H_f= 100 µm, exhibits the lowest CHF value of q''_{CHF}= 268 W/cm² that translates to a high two-phase thermal resistance of R''_{tp} of 8.7 mm²- °C/W. When the manifold spacing is reduced to W_{mani}= 550 µm, the CHF increases significantly to q''_{CHF}= 376 W/cm². This enhancement is attributed to the shorter wicking "spacing" between adjacent copper wire meshes. Additionally, reducing the manifold spacing does not adversely affect the superheat so overall the two-phase thermal resistance is lowered to R''_{tp}= 5 mm²- °C/W. Similarly, for the

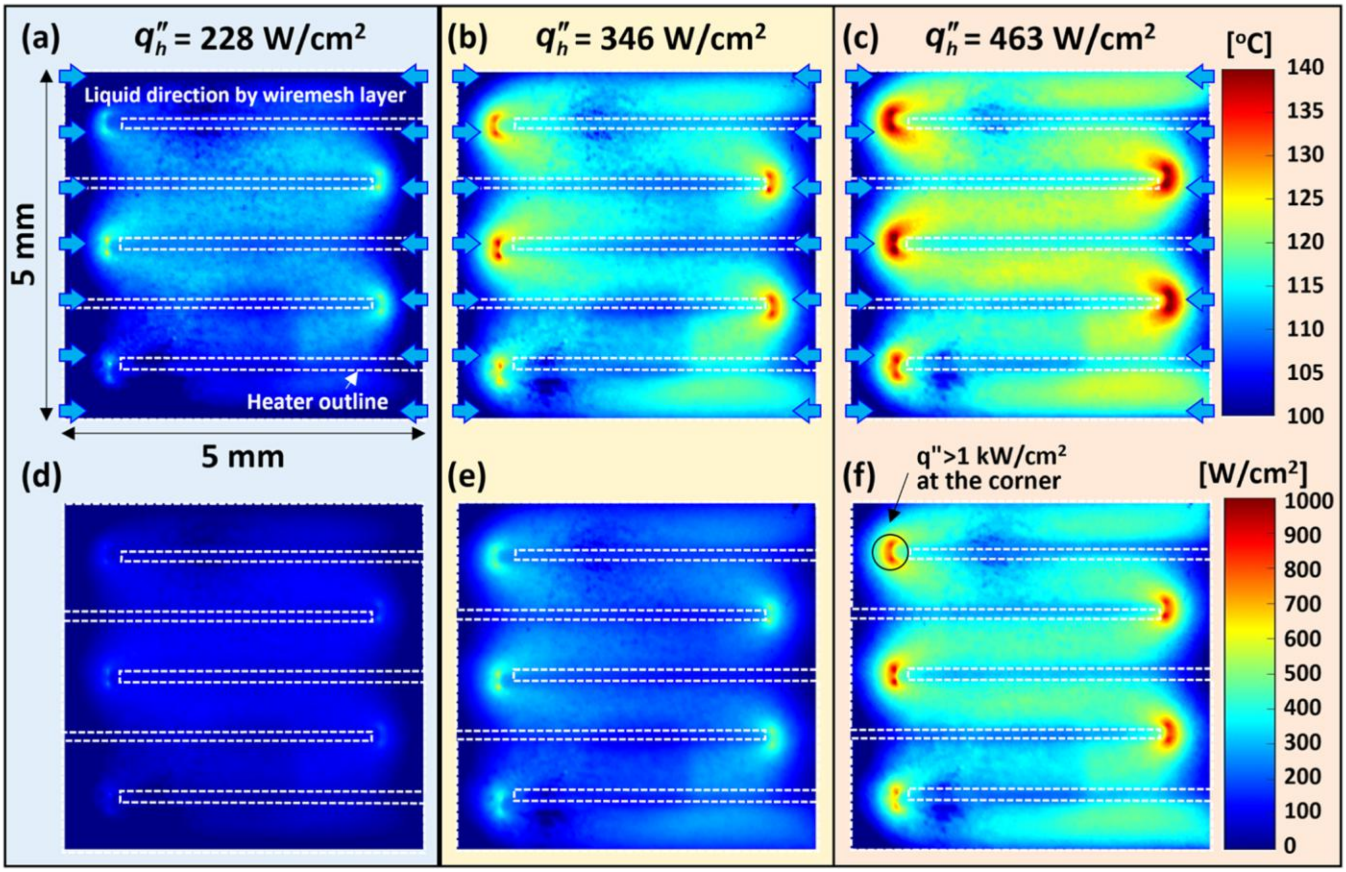

Fig. 4. (a)–(c) Wick (D11P29-M650) surface 2D temperature distribution (IR thermometry, resolution of 25 µm spacing per pixel) and (d)–(f) corresponding extracted heat flux distributions. T_{wick} is calculated from the 2D heater temperature map by assuming a one-dimensional temperature drop due to heat conduction across silicon substrate thickness and two-phase convection, referring to Eq. (2) and (5). Blue arrows indicate the water inflow from left/right direction through the copper wiremesh manifold, which explains the presence of slightly colder regions. The heat flux map at the wick surface is generated by multiplying the superheat temperature and the effective heat transfer coefficient on each pixel.

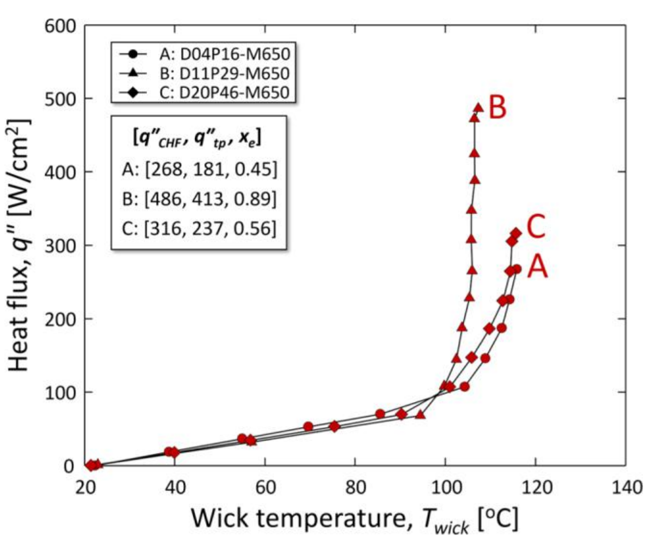

Fig. 5. Thermal performance (heat flux vs. spatially averaged wick temperature) for various pin fin geometries (cases A, B and C, listed in Table 1) at the highest flowrate level of 15 g/min and for W_{mani}=650 µm. The balance of viscous pressure in the wick and capillary pressure dictates the liquid supply level to evaporator wick that results in various CHF and superheat levels for wicks A, B and C. In general, a high level of critical heat flux (250 to 500 W/cm²) and a low level of superheat ΔT_{sat} (7 to 15 °C) is achieved.

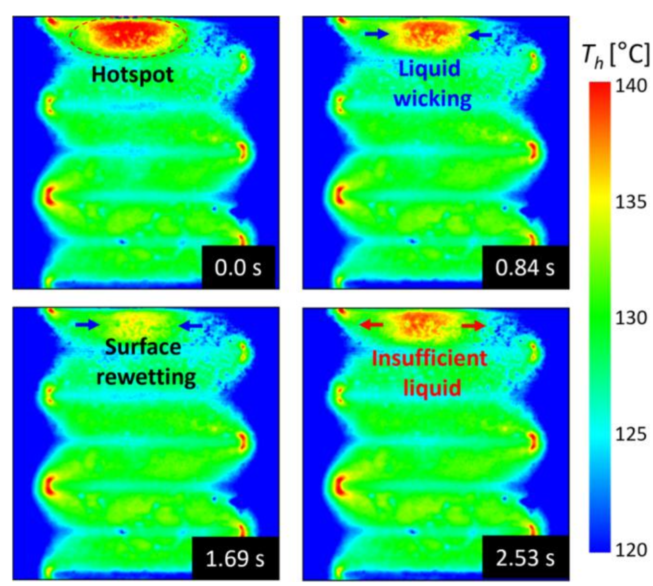

Fig. 6. Sequential heater temperature distribution captured by IR camera at near CHF of 268 W/cm² on D7P16-M650 (case A). A local hotspot, caused by insufficient liquid replenishment in the center region shows the unstable temperature fluctuation with high-temperature spikes.

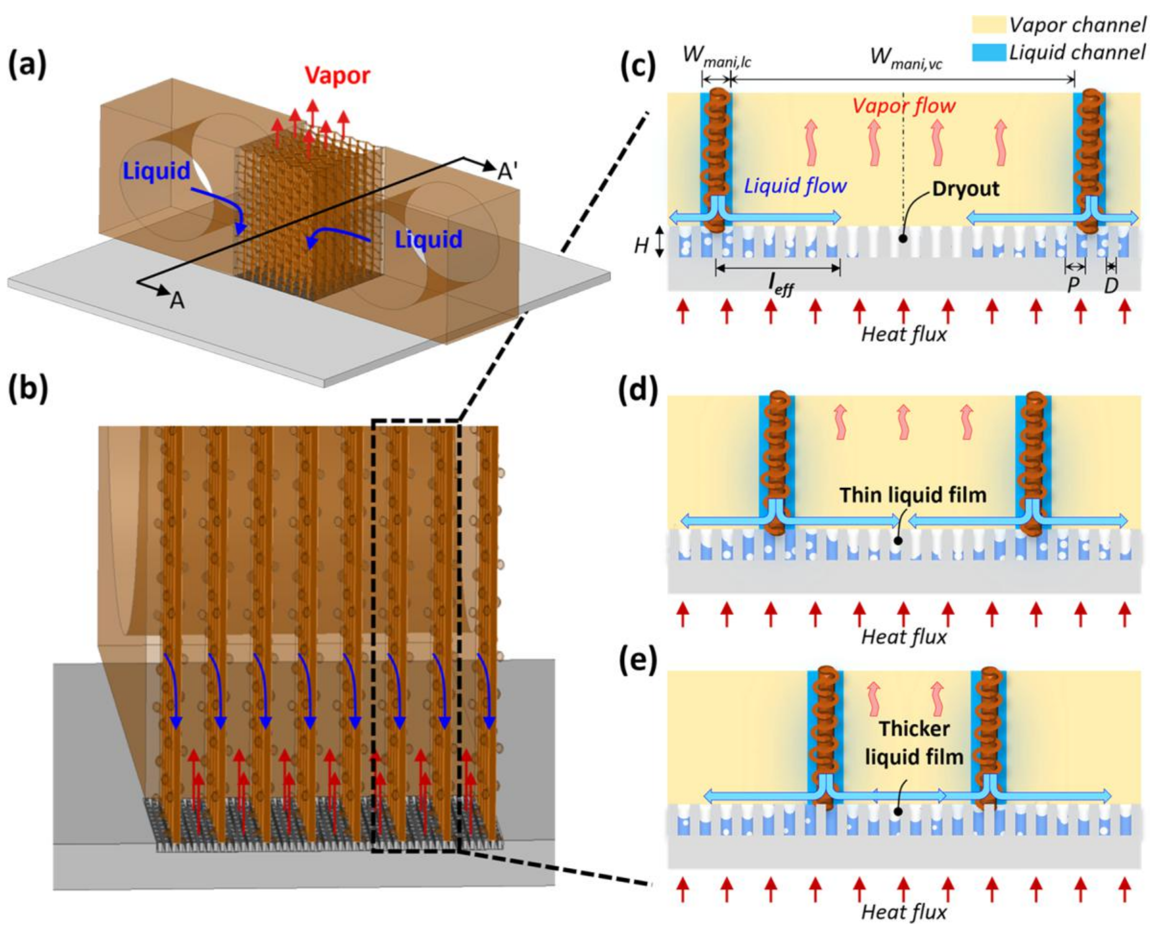

Fig. 7. The interplay of the effective wicking length and copper wire mesh 3D manifold spacing on the optimum design of the capillary-based microcooler. (a) Isometric view of full geometry of copper wiremesh manifold. (b) A close-up cross-sectional view along the A-A' plane. (c) $W_{mani,vc} > 2l_{eff}$, dry-out may occur at the center of the wick. (d) If $W_{mani,vc}$ is equal to or $<2l_{eff}$ (i.e., $W_{mani,vc} \leq 2l_{eff}$), higher CHF levels in the evaporator wick can be achieved, (e) further reducing the 3D manifold wiremesh spacing beyond $2l_{eff}$ unnecessarily adds to the number of copper wire mesh layers, which in turn reduces the effective area for capillary two-phase boiling [72], thereby reducing the total heat flux from the chip area.

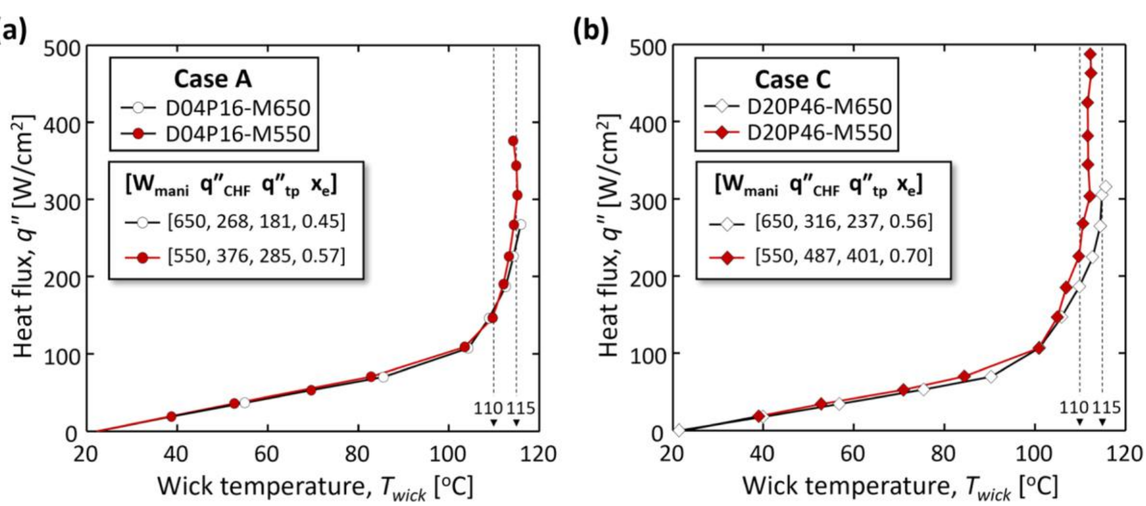

Fig. 8. Effect of wiremesh manifold spacing (650 μm and 550 μm) on the microcooler thermal performance. The smaller the spacing, the better performance achieved, indicating that the capillary wicking length for (a) D04P16 and (b) D20P46 is equal to or smaller than 225 μm.

D20P46 configuration, decreasing the manifold spacing from 650 μm to 550 μm reduces the thermal resistance by half to R''_{tp}= 3 mm²- °C/W, while the q''_{CHF} nearly doubled from 300 to 500 W/cm².

Among the three different wick types examined, the best performer, D11P29-M650, achieves the highest CHF and the lowest wick superheat temperature, resulting in the lowest two-phase thermal resistance of R''_{tp}= 1.8 mm²- °C/W. This superior performance is attributed to the synergistic effect of optimized wickability and permeability of the wick

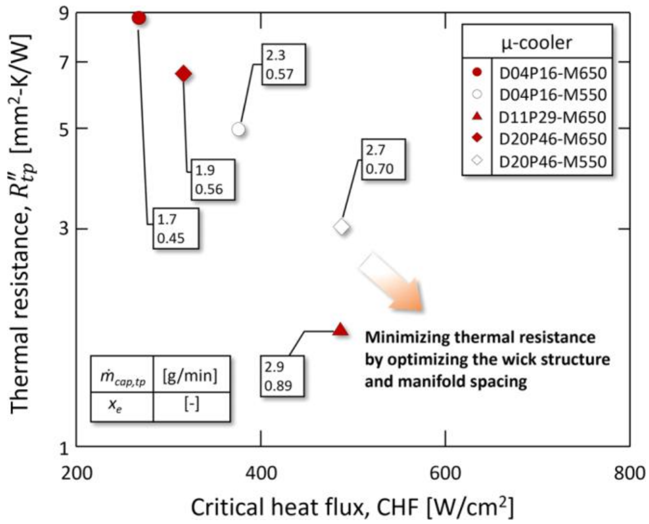

Fig. 9. Comparison of thermal performance and critical heat flux along with the geometrical combinations. Capillary-driven two-phase cooling demonstrates that a mass flow rate as low as $\dot{m}_{cap,tp}$ ~3 g/min can dissipate heat fluxes up to q''= 500 W/cm² while maintaining a high exit vapor quality of x_e ~0.9. Further reductions in thermal resistance and enhancements in allowable heat flux can be achieved by carefully tailoring the manifold spacing and the dimensions of the micropin fin wick structure.

structure [44,73,74]. Unfortunately, there is no data available for shorter wire mesh manifold spacing of W_{mani}= 550 μm, that could potentially result in even better performance (higher CHF and lower thermal resistance). Although not all possible combinations of geometrical factors were tested, the findings of this study provide valuable design recommendations for enhancing the two-phase thermal performance of capillary-based micro-coolers. Specifically, optimizing wick geometry and manifold spacing can significantly improve critical heat flux and reduce thermal resistance, thereby advancing the effectiveness of micro-cooler systems in thermal management applications.

Fig. 10 compares how thermal resistance scales with chip footprint for pump-based and capillary-based cooling schemes. As the footprint enlarges, thermal resistance inevitably rises. In pump-based coolers, a larger area fosters thicker thermal boundary layers and greater on-die temperature non-uniformity, both of which drive up the overall thermal resistance. In addition, in capillary-driven two-phase coolers, the available capillary-pressure margin diminishes with area, promoting early dry-out and CHF events, resulting in elevating thermal resistance.

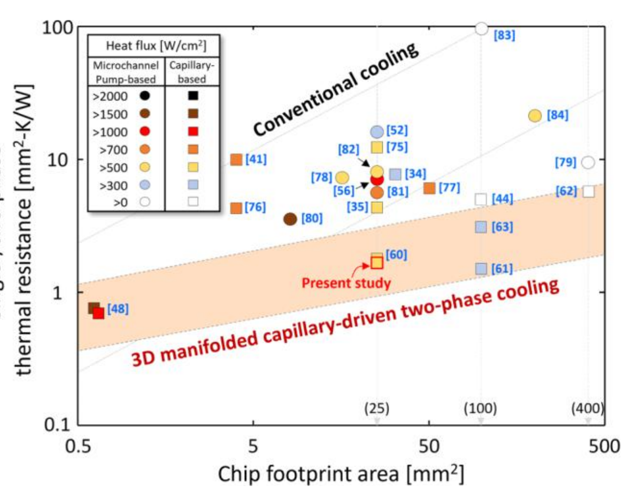

Fig. 10. Comparative study for thermal resistance scaling with chip footprint. Capillary-driven, two-phase cooling incorporating hierarchical manifolds [48, 60–63] including the present study suggest they have a potential to ~10× lower thermal resistance than those of conventional pump-based cooling methods [52,56,78–84] and other evaporation methods [34,35,41,44,75–77].

Consequently, conventional pump-driven single- and two-phase systems [52,56,78–84] span a broad grey band whose inclined slope reflects their strong flow-rate dependence. Evaporation driven solely by a wicking structure [34,35,41,44,75–77] falls within the same envelope and exhibits comparable performance. Around the common 25 mm² footprint—where most literature data cluster—thermal resistance typically lies between 4 and 16 mm²- °C/W. To break this limit, prior studies [48,60–63] and the present work incorporate a 3D manifold-based liquid-routing into capillary-driven cooling. The manifold sustains capillary-pressure margin, delaying dry-out and CHF, and thereby shifts the data into a distinct red band with a shallower thermal resistance slope. Notably, at 25 mm² the proposed wiremesh manifolded two-phase cooler achieves a superior thermal resistance of 1.5–1.6 mm²- °C/W, approximately an order of magnitude lower than that reported for conventional pump-driven cooling methods.

4. Conclusions

This study demonstrates the potential of a pumpless, capillary-driven microcooler that integrates thin-film boiling in silicon micropin fin wicks with a novel copper wiremesh 3D manifold using water as the working fluid. By systematically characterizing six variations of wick geometries (diameter, spacing, and height) in combination with two manifold designs (wiremesh spacings of 550 and 650 μm), we establish a clear link between geometry optimization and thermal performance. The results highlight the ability of this system to sustain a CHF level of ~500 W/cm² (chip area: 5 mm × 5 mm) with a low superheat of ΔT_{sat}= 7 °C, achieving a two-phase thermal resistance of R''_{tp} = 1.8 mm²- °C/W. Importantly, complete liquid–vapor phase separation was observed, reaching a vapor quality of x_e ≈ 0.9 under fully pumpless operation.

Beyond performance, the mechanical robustness of the proposed design is a critical advantage. Because the copper wiremesh 3D manifold is not bonded to the silicon wick evaporator, concerns about thermal mismatch are eliminated. This detachable configuration allows the flexible use of different wicking structures and manifold materials, opening opportunities for tailoring designs to specific applications without compromising reliability. The study also suggests that optimum performance can be achieved when the effective capillary wicking length is approximately half the spacing between the wiremesh arrays, providing a useful design guideline for future systems.

The findings provide a foundation for pushing the limits of cooling performance in microelectronics, with the potential to approach CHF levels near 1 kW/cm² and heat transfer coefficients exceeding 10^6 W/m²-°C. Future research directions will focus on further optimizing manifold plenums to reduce coolant drainage, improving wick permeability and effective conductivity, and exploring hierarchical manifold architectures for area scaling up to 30 mm × 30 mm. In parallel, the development of semi-empirical, physics-based models that integrate single-phase-evaporation, two-phase, and mixed-phase regimes will be essential to guide design. Finally, performance evaluation under sub-atmospheric and closed-loop conditions will bridge the gap toward practical implementation.

Taking together, this work highlights the critical role of advanced capillary-driven microcoolers in meeting the thermal demands of next-generation electronics. By enabling high heat flux removal, robust mechanical reliability, and scalable designs, such microcoolers offer a promising pathway for energy-efficient cooling of high-performance processors and data centers.

CRediT authorship contribution statement

Daeyoung Kong: Writing – review & editing, Writing – original draft, Methodology, Investigation, Formal analysis, Data curation. **Roman Giglio:** Writing – review & editing, Methodology, Investigation. **Muhammad R. Shattique:** Writing – review & editing, Methodology, Investigation. **Qianying Wu:** Writing – review & editing, Validation, Investigation. **Heungdong Kwon:** Writing – review & editing, Validation, Methodology. **James W. Palko:** Writing – review & editing, Validation, Supervision, Methodology, Investigation. **Hyoungsoon Lee:** Writing – review & editing, Validation, Investigation. **Ercan M. Dede:** Writing – review & editing, Validation, Methodology. **Mehdi Asheghi:** Writing – review & editing, Writing – original draft, Validation, Supervision, Project administration, Conceptualization. **Kenneth E. Goodson:** Supervision, Project administration, Funding acquisition, Conceptualization.

Declaration of competing interest

The authors declare that they have no known competing financial interests or personal relationships that could have appeared to influence the work reported in this paper.

Acknowledgments

We acknowledge financial support from the Advanced Research Projects Agency-Energy (ARPA-E) under the agreement DE-AR0001055, the International Cooperative R&D Program of the Korea Institute of Energy Technology Evaluation and Planning (KETEP), a grant funded by the Ministry of Trade, Industry & Energy, Korea. (Grant No RS-2024–00436521), and supported by CAU GPF Program through the Chung-Ang University in 2024 funded by BrainKorea21 Four.

Part of this work conducted at the Stanford Nanofabrication Facility (SNF) and Stanford Nanofabrication Shared Facilities (SNSF) with support of NSF (ECCS-2026822).

Supplementary materials

Supplementary material associated with this article can be found, in the online version, at doi:10.1016/j.ijmecsci.2025.110781.

Data availability

Data will be made available on request.

References

[1] International Energy Agency (IEA), Executive summary, global electricity demand rose moderately in 2023. 2024 https://www.iea.org/reports/electricity-2024/executive-summary.
[2] Nadjahi C, Louahlia H, Lemasson S. A review of thermal management and innovative cooling strategies for data center. Sust Comput 2018;19:14–28. https://doi.org/10.1016/j.suscom.2018.05.002.
[3] Zhang Y, Shan K, Li X, Li H, Wang S. Research and technologies for next-generation high-temperature data centers – state-of-the-arts and future perspectives. Renew Sust Energ Rev 2023;171:112991. https://doi.org/10.1016/j.rser.2022.112991.
[4] Kanbur BB, Wu C, Fan S, Duan F. System-level experimental investigations of the direct immersion cooling data center units with thermodynamic and thermoeconomic assessments. Energy 2021;217:119373. https://doi.org/10.1016/j.energy.2020.119373.
[5] Güğül GN, Gökçül F, Eicker U. Sustainability analysis of zero energy consumption data centers with free cooling, waste heat reuse and renewable energy systems: a feasibility study. Energy 2023;262:125495. https://doi.org/10.1016/j.energy.2022.125495.
[6] Li L, Zheng W, Wang X, Wang X. Data center power minimization with placement optimization of liquid-cooled servers and free air cooling. Sust Comput 2016;11:3–15. https://doi.org/10.1016/j.suscom.2016.02.001.
[7] Moazamigoodarzi H, Tsai PJ, Pal S, Ghosh S, Puri IK. Influence of cooling architecture on data center power consumption. Energy 2019;183:525–35. https://doi.org/10.1016/j.energy.2019.06.140.
[8] Nada SA, El-Zoheiry RM, Elsharnoby M, Osman OS. Experimental investigation of hydrothermal characteristics of data center servers' liquid cooling system for different flow configurations and geometric conditions. *Case stud.* Therm Eng 2021;27:101276. https://doi.org/10.1016/j.csite.2021.101276.
[9] Hnayno M, Chehade A, Klaba H, Bauduin H, Polidori G, Maalouf C. Performance analysis of new liquid cooling topology and its impact on data centres. Appl Therm Eng 2022;213:118733. https://doi.org/10.1016/j.applthermaleng.2022.118733.
[10] Birbarah P, Gebrael T, Foulkes T, Stillwell A, Moore A, Pilawa-Podgurski R, et al. Water immersion cooling of high power density electronics. Int J Heat Mass Transf 2020;147:118918. https://doi.org/10.1016/j.ijheatmasstransfer.2019.118918.
[11] Pambudi NA, Sarifudin A, Firdaus RA, Ulfa DK, Gandidi IM, Romadhon R. The immersion cooling technology: current and future development in energy saving. Alex Eng J 2022;61:9509–27. https://doi.org/10.1016/j.aej.2022.02.059.
[12] Alkasmoul FS, Almogbel AM, Shahzad MW, AJ A-. Thermal performance and optimum concentration of different nanofluids in immersion cooling in data center servers. Results Eng 2025;25:103699. https://doi.org/10.1016/j.rineng.2024.103699.
[13] Kim J, Choi H, Lee S, Lee H. Computational study of single-phase immersion cooling for high-energy density server rack for data centers. Appl Therm Eng 2025;264:125476. https://doi.org/10.1016/j.applthermaleng.2025.125476.
[14] Wu X, Yang J, Liu Y, Zhuang Y, Luo S, Yan Y, et al. Investigations on heat dissipation performance and overall characteristics of two-phase liquid immersion cooling systems for data center. Int J Heat Mass Transf 2025;239:126575. https://doi.org/10.1016/j.ijheatmasstransfer.2024.126575.
[15] Ding T, He ZG, Hao T, Li Z. Application of separated heat pipe system in data center cooling. Appl Therm Eng 2016;109:207–16. https://doi.org/10.1016/j.applthermaleng.2016.08.025.
[16] Ling L, Zhang Q, Yu Y, Liao S. A state-of-the-art review on the application of heat pipe system in data centers. Appl Therm Eng 2021;199:117618. https://doi.org/10.1016/j.applthermaleng.2021.117618.
[17] Wang H, Gan Y, Li R, Liu F, Li Y. Experimental study on the thermal performance of a liquid-cooled heat sink integrating heat pipes for dual CPU servers. Appl Therm Eng 2024;236:121851. https://doi.org/10.1016/j.applthermaleng.2023.121851.
[18] Zhang Y, Wang G, Wang X, Wang J, Xue H, Luan T. Performance and energy consumption study of a dual-evaporator loop heat pipe for chip-level cooling. Appl Therm Eng 2025;258:124757. https://doi.org/10.1016/j.applthermaleng.2024.124757.
[19] Wang N, Tian B, Wei Z, Guo Y, Dong Z, Ding D, et al. Experimental study of a dual-loop cooling system for data centers: a combined active and passive cooling approach. Energy 2025;333:137478. https://doi.org/10.1016/j.energy.2025.137478.
[20] Wang H, Bai P, Cai R, Luo Y, Chen X, Li S, et al. A hybrid vapor chamber heat sink incorporating a vapor chamber and liquid cooling channel with outstanding thermal performance and hydraulic characteristics. Energy Conv Manag 2021;244:114499. https://doi.org/10.1016/j.enconman.2021.114499.
[21] Zhou G, Zhou J, Huai X, Zhou F, Jiang Y. A two-phase liquid immersion cooling strategy utilizing vapor chamber heat spreader for data center servers. Appl Therm Eng 2022;210:118289. https://doi.org/10.1016/j.applthermaleng.2022.118289.
[22] Liao Y, Gan Y, Liu F, Li Y. Experimental study on the thermal performance of aluminum three-dimensional vapor chamber heat sink with a louvered-fin stacked evaporator wick for data center servers. Energy 2024;304:132037. https://doi.org/10.1016/j.energy.2024.132037.
[23] Luo F, Bai J, Yan C, Sun T, Li Y, Tang Y, et al. A novel aluminum boss vapor chamber with 3D bioinspired wick for thermal management in electronic chip. Appl Therm Eng 2025;259:124853. https://doi.org/10.1016/j.applthermaleng.2024.124853.
[24] Yuan X, Zhou X, Pan Y, Kosonen R, Cai H, Gao Y, et al. Phase change cooling in data centers: a review. Energy Build 2021;236:110764. https://doi.org/10.1016/j.enbuild.2021.110764.
[25] Alkrush AA, Salem MS, Abdelrehim O, Hegazi AA. Data centers cooling: a critical review of techniques, challenges, and energy saving solutions. Int J Refrig 2024;160:246–62. https://doi.org/10.1016/j.ijrefrig.2024.02.007.
[26] Megahed A. Experimental investigation of flow boiling characteristics in a cross-linked microchannel heat sink. Int J Multiph Flow 2011;37:380–93. https://doi.org/10.1016/j.ijmultiphaseflow.2010.12.002.
[27] Falsetti C, Magnini M, Thome JR. Flow boiling heat transfer and pressure drops of R1234ze(E) in a silicon micro-pin fin evaporator. J Electron Packag 2017;139:031008. https://doi.org/10.1115/1.4037152.
[28] Li C, Peterson GP, Wang Y. Evaporation/boiling in thin capillary wicks l—wick thickness effects. J Heat Transf 2006;128:1312–9. https://doi.org/10.1115/1.2349507.
[29] Wen R, Xu S, Lee Y-C, Yang R. Capillary-driven liquid film boiling heat transfer on hybrid mesh wicking structures. Nano Energy 2018;51:373–82. https://doi.org/10.1016/j.nanoen.2018.06.063.
[30] Kim H, Park Y, Kim H, Lee C, Jerng DW, Kim DE. Critical heat flux enhancement by single-layered metal wire mesh with micro and nano-sized pore structures. Int J Heat Mass Transf 2017;115:439–49. https://doi.org/10.1016/j.ijheatmasstransfer.2017.08.066.
[31] Zhou F, Zhou J, Li X, Chen Q, Huai X. Enhanced capillary-driven thin film boiling on cost-effective gradient wire meshes for high-heat-flux applications. Exp Therm Fluid Sci 2023;149:111018. https://doi.org/10.1016/j.expthermflusci.2023.111018.
[32] Chen G, Jiang X, Li Y, Bai J, Waqar Ali Shah S, Gao Y, et al. A highly efficient and sustainable heat sink via liquid film boiling in hybrid mesh with active liquid supply. Energy Conv Manag 2023;277:116688. https://doi.org/10.1016/j.enconman.2023.116688.
[33] Wu C, Tang Y, Zhu L, Sun Y, Zhang S, Yan C, et al. Enhanced capillary performance of nanostructures copper woven mesh wick for ultrathin heat pipes. Appl Therm Eng 2024;242:122476. https://doi.org/10.1016/j.applthermaleng.2024.122476.

[34] Semenic T, Catton I. Experimental study of biporous wicks for high heat flux applications. Int J Heat Mass Transf 2009;52:5113–21. https://doi.org/10.1016/j.ijheatmasstransfer.2009.05.005.
[35] Weibel JA, Garimella SV, North MT. Characterization of evaporation and boiling from sintered powder wicks fed by capillary action. Int J Heat Mass Transf 2010;53:4204–15. https://doi.org/10.1016/j.ijheatmasstransfer.2010.05.043.
[36] Sudhakar S, Weibel JA, Garimella SV. Experimental investigation of boiling regimes in a capillary-fed two-layer evaporator wick. Int J Heat Mass Transf 2019;135:1335–45. https://doi.org/10.1016/j.ijheatmasstransfer.2019.03.008.
[37] Lohan DJ, Sarma B, Joshi SN, Dede EM, Soto A, Sudhakar S, et al. Thermal performance of a pump-assisted capillary loop cooler. J Therm Sci Eng Appl 2024;16:091006. https://doi.org/10.1115/1.4065619.
[38] Zhou Y, Liu J, Ni Y, Cui Q, Yang X, Wei J, et al. Performance of a novel loop heat pipe coupled with micro vapor-driven jet injector – an experimental and numerical study. Int J Heat Mass Transf 2024;231:125853. https://doi.org/10.1016/j.ijheatmasstransfer.2024.125853.
[39] Kim S, Kim HD, Kim H, Ahn HS, Jo H, Kim J, et al. Effects of nano-fluid and surfaces with nano structure on the increase of CHF. Exp Therm Fluid Sci 2010;34:487–95. https://doi.org/10.1016/j.expthermflusci.2009.05.006.
[40] Li Q, Wang W, Oshman C, Latour B, Li C, Bright VM, et al. Enhanced pool boiling performance on micro-, nano-, and hybrid-structured surfaces. Volume 10. Heat and mass transport processes, parts a and b 2011:633–40. https://doi.org/10.1115/IMECE2011-64921.
[41] Cai Q, Chen Y-C. Investigations of biporous Wick structure dryout. J Heat Transf 2012;134:021503. https://doi.org/10.1115/1.4005099.
[42] Chun J, Xu C, Li Q, Chen Y, Zhao Q, Yang W, et al. Microscopic observation of preferential capillary pumping in hollow Nanowire bundles. Langmuir 2022;38:352–62. https://doi.org/10.1021/acs.langmuir.1c02647.
[43] Zhang Y, Zhao X, Li J, Wang Q, Zhong D, Zheng D, et al. Manipulating thin film boiling to achieve record-breaking high heat flux. Int J Heat Mass Transf 2024;224:125308. https://doi.org/10.1016/j.ijheatmasstransfer.2024.125308.
[44] Ćoso D, Srinivasan V, Lu M-C, Chang J-Y, Majumdar A. Enhanced heat transfer in biporous wicks in the thin liquid film evaporation and boiling regimes. J Heat Transf 2012;134:101501. https://doi.org/10.1115/1.4006106. D. Ćoso, V. Srinivasan, M.-C. Lu, J.-Y. Chang, A. Majumdar, Enhanced heat transfer in biporous wicks in the thin liquid film evaporation and boiling regimes, *J. Heat Transf.* 134 (2012) 101501.
[45] Luo K, Foysal F, Chang W, Santi E, Li C. Scalable capillary-pin-fin structure enabled efficient flow boiling. Appl Phys Lett 2024;125:024104. https://doi.org/10.1063/5.0198135.
[46] Lin Y, Kwon H, Chen H, Gupta MP, Degner M, Asheghi M, et al. The impact of liquid supply delivery methods on the thermal performance of a capillary-based two-phase micro-cooler for the power electronics. In: 2024 23rd IEEE Intersociety Conference on Thermal and Thermomechanical Phenomena in Electronic Systems (ITherm). Aurora, CO, USA: IEEE; 2024. p. 1–8. https://doi.org/10.1109/ITherm55375.2024.10709623.
[47] Li P, Zou Q, Liu X, Yang R. A heat transfer model for liquid film boiling on micro-structured surfaces. Natl Sci Rev 2024;11:nwae090. https://doi.org/10.1093/nsr/nwae090.
[48] Palko JW, Zhang C, Wilbur JD, Dusseault TJ, Asheghi M, Goodson KE, et al. Approaching the limits of two-phase boiling heat transfer: high heat flux and low superheat. Appl Phys Lett 2015;107:253903. https://doi.org/10.1063/1.4938202.
[49] Zhang C, Palko JW, Barako MT, Asheghi M, Santiago JG, Goodson KE. Enhanced capillary-fed boiling in copper inverse opals via template sintering. Adv Funct Mater 2018;28:1803689. https://doi.org/10.1002/adfm.201803689.
[50] Yang Y, Du J, Li M, Li W, Wang Q, Wen B, et al. Embedded microfluidic cooling with compact double H type manifold microchannels for large-area high-power chips. Int J Heat Mass Transf 2022;197:123340. https://doi.org/10.1016/j.ijheatmasstransfer.2022.123340.
[51] Wei T, Hazra S, Lin Y, Gupta MP, Degner M, Asheghi M, et al. Numerical study of large footprint (24 × 24 mm2) silicon-based embedded microchannel three-dimensional manifold coolers. J Electron Packag 2023;145:021008. https://doi.org/10.1115/1.4055468.
[52] Jung KW, Kharangate CR, Lee H, Palko J, Zhou F, Asheghi M, et al. Embedded cooling with 3D manifold for vehicle power electronics application: single-phase thermal-fluid performance. Int J Heat Mass Transf 2019;130:1108–19. https://doi.org/10.1016/j.ijheatmasstransfer.2018.10.108.
[53] Kong D, Kwon H, Lee H, Lee H, Asheghi M, Goodson KE. In: Computational Fluid Dynamics (CFD) Modeling and Optimization of Large-Scale (3 cm X 3 cm) Silicon-Based Embedded Microchannels With 3D Manifold Micro-Coolers. ASME 2024 International Technical Conference and Exhibition on Packaging and Integration of Electronic and Photonic Microsystems. San Jose, California, USA: American Society of Mechanical Engineers; 2024. https://doi.org/10.1115/IPACK2024-141064. V001T03A014.
[54] Palko JW, Lee H, Zhang C, Dusseault TJ, Maitra T, Won Y, et al. Extreme two-phase cooling from laser-etched diamond and conformal, template-fabricated microporous copper. Adv Funct Mater 2017;27:1703265. https://doi.org/10.1002/adfm.201703265.
[55] Singh H, Mandel R, Sarmiento A, Ohadi M. Thermal management of high flux electronics using film evaporation with an enhanced fluid delivery system (FEEDS). Int Commun Heat Mass Transf 2023;148:107008. https://doi.org/10.1016/j.icheatmasstransfer.2023.107008.
[56] Kong D, Kwon H, Jang B, Kwon H-J, Asheghi M, Goodson KE, et al. Extreme heat flux cooling from functional copper inverse opal-coated manifold microchannels. Energy Conv Manag 2024;315:118809. https://doi.org/10.1016/j.enconman.2024.118809.
[57] Dede EM, Zhang C, Wu Q, Seyedhassantehrani N, Shattique M, Roy S, et al. Techno-economic feasibility analysis of an extreme heat flux micro-cooler. iScience 2023;26:105812. https://doi.org/10.1016/j.isci.2022.105812.
[58] Giglio R, Shattique MR, Dede EM, Narumanchi S, Asheghi M, Goodson KE, et al. Porous mesh manifold for enhanced boiling performance. Appl Therm Eng 2025;260:124918. https://doi.org/10.1016/j.applthermaleng.2024.124918.
[59] Shattique MR, Giglio R, Dede EM, Narumanchi S, Asheghi M, Goodson KE, et al. Permeability of single-layer-free-standing meshes at varying capillary pressure via a novel method. Adv Mater Interfaces 2023;10:2300326. https://doi.org/10.1002/admi.202300326.
[60] Kwon H, Wu Q, Kong D, Hazra S, Jiang K, Narumanchi S, et al. Capillary-enhanced two-phase micro-cooler using copper-inverse-opal wick with silicon microchannel manifold for high-heat-flux cooling application. Int Commun Heat Mass Transf 2024;156:107592. https://doi.org/10.1016/j.icheatmasstransfer.2024.107592.
[61] Kwon H, Wu Q, Kong D, Hazra S, Jiang K, Ahn C, et al. Development of a hybrid single/two-phase capillary-based micro-cooler using copper inverse opals wick with silicon 3D manifold for high-heat-flux cooling application. In: 2024 23rd IEEE Intersociety Conference on Thermal and Thermomechanical Phenomena in Electronic Systems (ITherm). Aurora, CO, USA: IEEE; 2024. p. 1–10. https://doi.org/10.1109/ITherm55375.2024.10708971.
[62] Kwon H, Kong D, Lee H, Palko J, Dede EM, Asheghi M, et al. Scalable large-area two-phase capillary-enhanced micro-cooler using silicon microchannel fin array with 3D silicon manifold for high-heat-flux electronics cooling application. In: ASME 2024 International Technical Conference and Exhibition on Packaging and Integration of Electronic and Photonic Microsystems. San Jose, California, USA: American Society of Mechanical Engineers; 2024. https://doi.org/10.1115/IPACK2024-140613. V001T03A006.
[63] Li P, Liu X, Wen R, Yang R. Hierarchical ordered perforated surface for highly efficient liquid film boiling. Cell Rep Phys Sci 2025;6:102601. https://doi.org/10.1016/j.xcrp.2025.102601.
[64] Lu L, Tao B, Yang S, Zhong Y, Xie Y. Enhanced capillary-driven thin film boiling through superhydrophilic mesh wick structure. Int J Therm Sci 2025;212:109782. https://doi.org/10.1016/j.ijthermalsci.2025.109782.
[65] Lin Y, Wei T, Moy WJ, Chen H, Gupta MP, Degner M, et al. Multi-level embedded three-dimensional manifold microchannel heat sink of aluminum nitride direct bonded copper for the high-power electronic module. J Electron Packag 2024;146:011006. https://doi.org/10.1115/1.4062384.
[66] Hazra S, Wei T, Lin Y, Asheghi M, Goodson KE, Gupta MP, et al. Parametric design analysis of a multi-level 3D manifolded microchannel cooler via reduced order numerical modeling. Int J Heat Mass Transf 2022;197:123356. https://doi.org/10.1016/j.ijheatmasstransfer.2022.123356.
[67] Lin Y, Kwon H, Chen H, Gupta MP, Degner M, Asheghi M, et al. Development of a hybrid capillary-driven single-phase and two-phase micro-cooler for power electronics cooling. IEEE Trans Compon Packag Manufact Technol 2024;14:810–23. https://doi.org/10.1109/TCPMT.2024.3369002.
[68] Kwon H., Giglio R., Kong D., Shattique M.R., Lee H., Palko J., Dede E.M., Asheghi M., Goodson K.E., Capillary-driven two-phase cooler for high-heat-flux electronics using copper wiremesh manifold and enhanced copper inverse opal wick heat sink. Available at SSRN: https://ssrn.com/abstract=5271612.
[69] Dhillon NS, Buongiorno J, Varanasi KK. Critical heat flux maxima during boiling crisis on textured surfaces. Nat Commun 2015;6:8247. https://doi.org/10.1038/ncomms9247.
[70] Seo H, Chu JH, Kwon S-Y, Bang IC. Pool boiling CHF of reduced graphene oxide, graphene, and SiC-coated surfaces under highly wettable FC-72. Int J Heat Mass Transf 2015;82:490–502. https://doi.org/10.1016/j.ijheatmasstransfer.2014.11.019.
[71] Byon C, Kim SJ. The effect of meniscus on the permeability of micro-post arrays. J Micromech Microeng 2011;21:115011. https://doi.org/10.1088/0960-1317/21/11/115011.
[72] Wu Q, Kwon H, Asheghi M, Goodson KE. Design of manifolded 3D μ-coolers enabling high heat flux capillary-driven boiling over large areas. IEEE Trans Compon Pack Manuf Technol 2024:1. https://doi.org/10.1109/TCPMT.2024.3410210.
[73] Sudhakar S, Weibel JA, Zhou F, Dede EM, Garimella SV. The role of vapor venting and liquid feeding on the dryout limit of two-layer evaporator wicks. Int J Heat Mass Transf 2020;148:119063. https://doi.org/10.1016/j.ijheatmasstransfer.2019.119063.
[74] Fang J, Cheng H, Fan D. Enhanced heat transfer using wafer-scale crack-free well-ordered porous structure surface. Int Commun Heat Mass Transf 2023;148:107018. https://doi.org/10.1016/j.icheatmasstransfer.2023.107018.
[75] Hwang GS, Fleming E, Carne B, Sharratt S, Nam Y, Dussinger P, et al. Multi-artery heat-pipe spreader: lateral liquid supply. Int J Heat Mass Transf 2011;54:2334–40. https://doi.org/10.1016/j.ijheatmasstransfer.2011.02.029.
[76] Nam Y, Sharratt S, Cha G, Ju YS. Characterization and modeling of the heat transfer performance of nanostructured Cu micropost wicks. J Heat Transf 2011;133:101502. https://doi.org/10.1115/1.4004168.
[77] Feng T, Pei Y, Zhang H, Asai B, Dong G, Joshi A, et al. High-flux and stable thin-film evaporation from fiber membranes with interconnected pores. Joule 2025:101975. https://doi.org/10.1016/j.joule.2025.101975.
[78] Everhart L, Jankowski N, Geil B, Bayba A, Ibitayo D, McCluskey P. Manifold microchannel cooler for direct backside liquid cooling of SiC power devices. In: ASME 5th International Conference on Nanochannels, Microchannels, and Minichannels. Puebla, Mexico: ASMEDC; 2007. p. 285–92. https://doi.org/10.1115/ICNMM2007-30190.

[79] Escher W, Brunschwiler T, Michel B, Poulikakos D. Experimental investigation of an ultrathin manifold microchannel heat sink for liquid-cooled chips. J Heat Transf 2010;132. https://doi.org/10.1115/1.4001306.

[80] van Erp R, Soleimanzadeh R, Nela L, Kampitsis G, Matioli E. Co-designing electronics with microfluidics for more sustainable cooling. Nature 2020;585: 211–6. https://doi.org/10.1038/s41586-020-2666-1.

[81] Drummond KP, Back D, Sinanis MD, Janes DB, Peroulis D, Weibel JA, et al. A hierarchical manifold microchannel heat sink array for high-heat-flux two-phase cooling of electronics. Int J Heat Mass Transf 2018;117:319–30. https://doi.org/10.1016/j.ijheatmasstransfer.2017.10.015.

[82] Back D, Drummond KP, Sinanis MD, Weibel JA, Garimella SV, Peroulis D, et al. Design, fabrication, and characterization of a compact hierarchical manifold microchannel heat sink array for two-phase cooling. IEEE Trans Compon Packag Manuf Technol 2019;9:1291–300. https://doi.org/10.1109/TCPMT.2019.2899648.

[83] Yang M, Li M-T, Hua Y-C, Wang W, Cao B-Y. Experimental study on single-phase hybrid microchannel cooling using HFE-7100 for liquid-cooled chips. Int J Heat Mass Transf 2020;160:120230. https://doi.org/10.1016/j.ijheatmasstransfer.2020.120230.

[84] Battaglia F, Singer F, Deisenroth DC, Ohadi MM. Experimental characterization of two-phase cooling of power electronics in thermosiphon and forced convection modes. J Electron Packag 2021;143:031006. https://doi.org/10.1115/1.4049564.